Nanowires of lead-methylamine iodide (CH$_3$NH$_3$PbI$_3$) prepared by low temperature solution-mediated crystallization

E. Horváth[1]*, M. Spina[1], Zs. Szekrényes[2], K. Kamarás,[2] R.Gaal,[1] D. Gachet[3], L. Forró[1]

[1]Laboratory of Physics of Complex Matter (LPMC), Ecole Polytechnique Fédérale de Lausanne, 1015 Lausanne, Switzerland

[2]Institute for Solid State Physics and Optics, Wigner Research Centre for Physics, Hungarian Academy of Sciences, 1525 Budapest, Hungary

[3] Attolight AG, Innovation Park, 1015 Lausanne, Switzerland

KEYWORDS

Perovskite, solar cell, photodetector, grain boundary, crystallization.

ABSTRACT

We report the synthesis of lead-methylamine iodide ($CH_3NH_3PbI_3$) nanowires by a low temperature solution processed crystallization using a simple slip-coating method. The anisotropic particle shape exhibits advantages over nanoparticles in terms of charge transport under illumination. These results provide a basis for solvent-mediated tailoring of structural properties like the crystallite size and orientation in trihalide perovskite thin films, which once implemented into a device, may ultimately result in an enhanced charge carrier extraction.

MAIN TEXT

Perovskites, the structural analogues of the natural crystal of calcium titanium oxide, cover a broad range of versatile materials, which have potential applications in multiple fields such as superconductors[1], sensors[2], fuel cells[3], ferroelectrics[4] and thermoelectrics[5]. The recently

rediscovered, half-century old members of this family[6], organolead halide perovskites, turned

out to be promising components of next generation solar cells[7]. Incorporated as a light

harvesters in mesoscopic solar cells, a remarkable power conversion efficiency of 16.2 % was

demonstrated in lab-scale devices[8]. It has been shown that aside from the role of the light

absorber, the organolead halide perovskites can be viewed both as electron and hole

transporting media due to their ambipolar charge transport character[9]. So far, the highest

solar-to-electric conversions have been reached with two main compounds (the $CH_3NH_3PbI_3$

and $CH_3NH_3PbI_{3-x}Cl_x$, abbreviated as $MAPbI_3$ and $MAPbI_{3-x}Cl_x$) showing minor alterations

in halide content[10,11]. These are direct band gap semiconductors with a high absorption

coefficient, a favorable band gap of 1.5-1.65 eV and electron-hole diffusion length ranging

from $\approx$100nm to $\approx$1 micron[12,8, 13, 14]. However, the structural and electronic differences

between the two materials, as well as the exact role of the Cl anions have yet to be

undoubtedly determined by the scientific community. Colella et. al.[15] observed that

incorporation of Cl as a dopant dramatically improves the charge transport within the

perovskite layer. It has also been described that the Cl inclusion enhances the granular

morphology resulting in a more homogenous current production probed by electron beam-

induced current (EBIC) method[16]. Very recently, by inserting formamidinium cations into a

lead iodide structure, nearly cubic phase (band gap ≈1.43 eV) perovskite was reported, with an absorption edge broadened by 30 nm as compared to $MAPbI_3$[17]. These findings validate the bandgap engineering strategies, where the bandgap of the material might be efficiently tuned by choosing the halide anion and the organic amide constituent[18,19,20]. One of the key aspects towards a low-cost technology capable of competing with the established silicon technology lies in the material`s low temperature solution processability. The current approach is based on a single step deposition of a mixture of PbX_2 and CH_3NH_3X (X is a halide anion) in a common solvent or sequential deposition of the constituents from a solution onto a mesopourous scaffold[21,22]. Rapid crystallization of the perovskite has been observed during the spin-coating process. In order to obtain an optimized device performance, very often a post-annealing treatment is required. Recent results[23] demonstrated an efficiency of 15 % on devices entirely processed below 150 °C. The general observation is that minor alterations of the applied processing parameters may lead to dramatically different device performances. This indicates that it is critical to have fine control over the nucleation and crystal growth of the $MAPbI_3$. In their effort to control the morphology of the trihalide perovskite films, Eperon et al.[24] showed that the highest photocurrents were attainable only with the highest perovskite surface coverage. This prior work suggests that the final

crystalline morphology depends mainly on the dynamics of annealing, which will ultimately govern the solvent evaporation, pore voiding or closing and the film thickness. Liu and co-workers reported[25] that the solution-cast films onto a compact TiO_2-layer over an FTO-coated glass inhomogeneously covered the substrate and that it was composed of crystalline 'platelets' with a length on the scale of tens of micrometres. The crystallite sizes determined from X-ray diffraction were larger than 400 nm. On the other hand, studies based on electron microscopy observations report the presence of small, ~6 nm nanoparticles supported by surface-modified mesoporous TiO_2 film prepared by solution processing.[26] As is well known, the dimensionality and morphology of crystallites may have a striking influence on their chemical and physical properties. Under most circumstances, nano- and micron-sized particles with isotropic particle shapes have been observed. This suggests that the crystallites tend to grow uniformly along the three major crystallographic directions. This can be easily accepted, since $MAPbI_3$ more likely crystallizes in a cubic structure, therefore in principle there should be no crystallographic driving force for anisotropic growth. Surprisingly, we found that some solvents induce highly anisotropic crystallization of $MAPbI_3$. To the authors' knowledge, no 1D form of organolead halide perovskites has been observed to date.

Here we report the synthesis of two sets of MAPbI$_3$ nanowires with mean diameter of 50 and 400 nm and length up to 10 µm. They were prepared through a simple slip-coating approach. The one-dimensional form of MAPbI$_3$ could have unique optical and electrical properties. The feasibility of anisotropic growth of organolead halide perovskites opens up a new strategy towards the realization of low-temperature, solution processed films with controlled morphology.

Synthesis

Saturated solution of MAPbI$_3$ in dimethylformamide (DMF) was dropped onto a glass microscope slide and covered with a second glass slide so that the excess yellow solution squeezed out; the remaining solution formed a homogenous liquid film between the glass plates (Fig 1 a-c, details of the synthesis can be found in the Supporting Information). The excess of MAPbI$_3$ solution was removed from the sides by soaking with a tissue. Next, the bottom substrate was held in place while gradually sliding the upper glass plate, exposing the thin liquid film to air. Solvent evaporation from the uncovered surface caused an instantaneous yellow to brown-red color change.
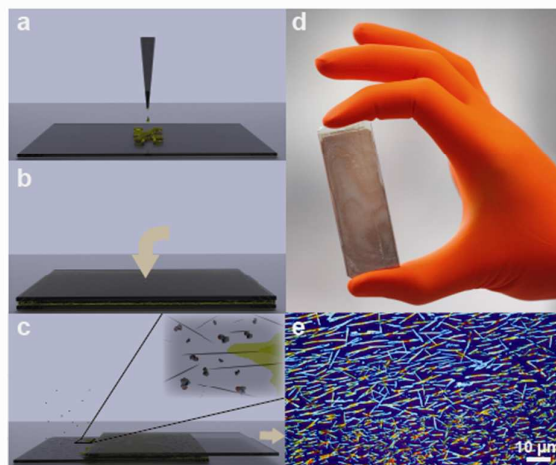
Figure 1. Schematic illustration of the low temperature slip-coating process for the fabrication of filiform lead-methylamine iodide perovskite thin films (a-c). Photo of the coating formed on a microscope glass slide (d). Optical microscopy image of filiform crystallites grown on SiO_2/Si substrate (e).

Optical microscopy was performed to confirm the crystallization of the solid. Unexpectedly, instead of a granular film composed of isotropic crystallites, a network of several micron long wire-like objects was observed, some of them pointing in the direction of

sliding of the two glass plates (Fig 1 d-e). The filiform morphology was further confirmed

using TEM, SEM and AFM measurements.

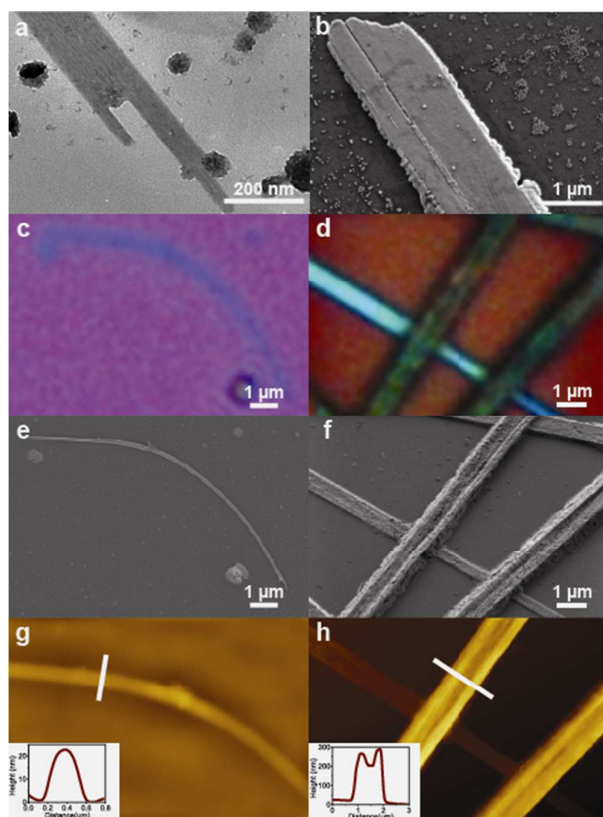**Figure 2.** Morphological parameters of filiform MAPbI$_3$ crystallites. TEM image of a MAPbI$_3$ (a),

Optical microscope images of individual MAPbI$_3$ nanowire (c-d). SEM image of micron-sized

MAPbI$_3$ filaments grown on SiO$_2$/Si surface (b, e, f). AFM images and height profiles. The white lines denote the corresponding cross-section profiles shown in the insets (g-h). Note that for Figures c-g and d-h the same zones of the surfaces are imaged.

The width of the nanowires varied between 50 and 200 nm and they had lengths up to 16 microns. The height of the crystallites was determined from AFM measurements displaying a range from ultrathin (~9 nm) to several tens of nanometers thick (~90 nm) scale. The formation of a small number of aggregates of ~10 nm sized isotropic crystallites was also observed, as can be seen on TEM and SEM micrographs (Fig 2 a, b). These particles were homogeneously dispersed on the SiO$_2$ surface and attached to the wall of larger nanowires (Fig 2 b.). Increasing the MAPbI$_3$ solution volume-to-surface ratio during the slip-coating process yields larger, sub-micron sized whiskers (Fig 2 b, d, f, h, experimental details in the Supporting Information). Unlike the thinner wires that have a flat surface, some of these thicker crystallites possess a U-shape void along their surface. The size distribution of nanowires (read from optical, AFM and SEM images) prepared by two solution volumes is shown in Figure 3. We experienced that parameters such as solvent concentration,

temperature, fluid philicity/phobicity, sliding speed, etc. influence the kinetics of crystallization. We assume that the optimized combination of these parameters could result in a major product having well-controlled surface density, crystal habit, aspect ratio, size-distribution and even orientation on a given substrate.
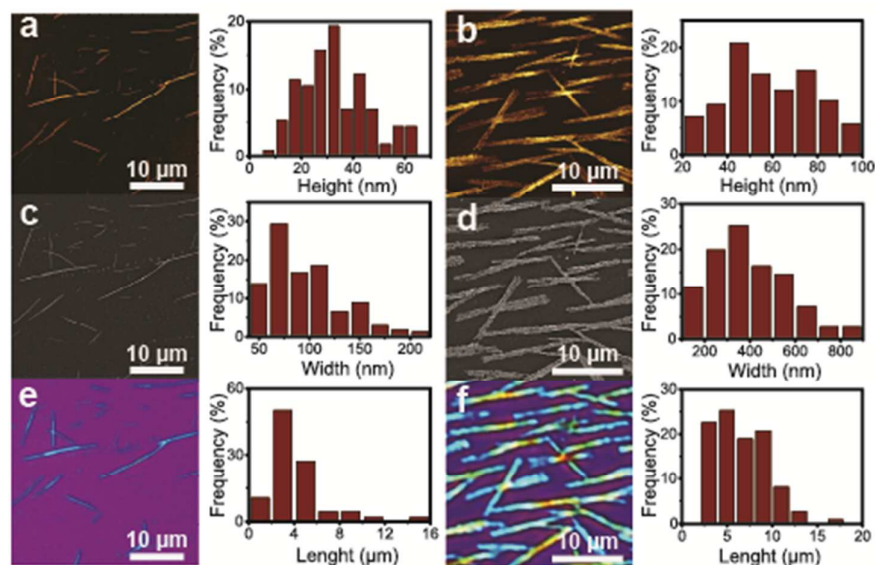
Figure 3. Size distribution of two sets of nanowires of MAPbI$_3$. The height has been determined by AFM (a, b) while the width and length have been obtained by SEM (c, d) and optical microscopy (e, f) images.

1
2
3
4
5
6
7
8
9
10
11
12
13
14
15
16
17
18
19
20
21
22
23
24
25
26
27
28
29
30
31
32
33
34
35
36
37
38
39
40
41
42
43
44
45
46
47
48
49
50
51
52
53
54
55
56
57
58
59
60

The elemental composition of the anisotropic crystallites was analyzed by EDX. The presence of lead and iodine was readily confirmed, while the low atomic number carbon and nitrogen cannot be reliably quantified by EDX (Supplementary Figure S3). The Pb:I atomic percent ratio was found to be 25:75. To gain more insight into the structure of the nanowires XRD, Raman and infrared spectroscopies were performed. The XRD diffractogram shows high intensity diffraction peaks at 2 Theta 14 ° (110) and 28.4 ° (220), which were identified as the characteristic peaks of the cubic $MAPbI_3$ phase[27]. The presence of the low intensity peak at 12.54° is assigned to a PbI_2 phase which presumably formed as a result of the humidity-induced partial decomposition of $MAPbI_3$ during the PXRD measurement. The presence of two major reflection peaks suggests that the crystallites are highly oriented along the (110) direction. Raman spectra recorded on filiform crystallites are also in accordance with the reported Raman modes of $MAPbI_3$[28]. The cathodoluminescence spectrum of filiform nanoparticles shows a single peak centered at ~770 nm, ~1.61eV (FigS7). This peak position corresponds well with the band gap reported of $MAPbI_3$ perovskites (1.5 eV to 1.6 eV). Furthermore, Fourier Transform Infrared Spectroscopy (FTIR) spectra show a close correspondence in the vibration modes of filiform crystallites and bulk single crystal suggesting identical chemical composition ($CH_3NH_3PbI_3$).

The central question is where does the directionality of the perovskite growth stem from? The role of the solvent in the nanowire formation was investigated by changing the solvent. The same protocol was repeated by replacing dimethylformamide (DMF) by gamma-butyrolactone (GBL), another commonly used solvent of organolead halide perovskites. Due to GBL's higher boiling point the evaporation was much slower, and ca. 350 K heat treatment was required to evaporate the solvent. Clearly, no anisotropic growth was taking place during the slip-coating process from GBL solution. Thus, we assume that the use of DMF is the key step, and therefore a unique role of DMF as a growth-directing agent is suggested. It is not clear yet whether DMF specifically affects the crystallization kinetics of the lead iodide framework or if the directional growth is due to an internal complex or adduct formation with the methylamine group. Currently we are assuming the second as a working hypothesis. The elucidation of the exact role of DMF on the formation of different solvatomorphs will be the subject of further studies.

Testing of photoresponse of the nanowires

The major interest in $MAPbI_3$ is its high sensitivity to visible-light, which together with its high photovoltage of about 1.1 V are the basic ingredients for efficient solar-to-electric

1
2
3
4
5
6
7
8
9
10
11
12
13
14
15
16
17
18
19
20
21
22
23
24
25
26
27
28
29
30
31
32
33
34
35
36
37
38
39
40
41
42
43
44
45
46
47
48
49
50
51
52
53
54
55
56
57
58
59
60

energy conversion[29]. These advantageous characteristics will certainly be explored in other device-oriented research, like photodetection and solid state lasers[30]. The elucidation of the morphology-dependent photoconductive performance could have a consequence on the development of more efficient devices. So far, the intrinsic photoconductive properties measured by standard contact methods have not even been reported for the bulk samples. Here, we demonstrate the first results showing that one can make efficient photodetectors based on nanowires of $MAPbI_3$. In addition, these findings are compared to the photodetection of a thin film of spin coated $MAPbI_3$ frequently used in photovoltaic devices.

The devices were fabricated by slip-coating nanowires of different sizes of $MAPbI_3$ onto a highly p-doped silicon substrate with 300 nm SiO_2 on top. 100-nm-thick Pt contacts were deposited by e-beam evaporation through a microfabricated hard mask. The fabricated devices have a width of 100 μm and a length varying between 5 μm and 50 μm. The sketch and the optical image of a device are shown in Figure 4a and 4b.
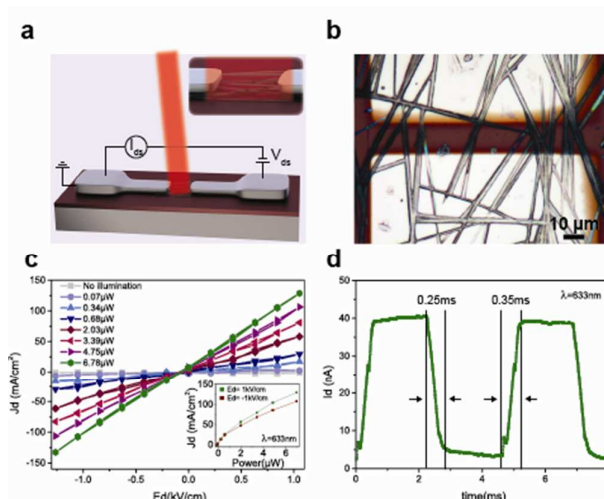
Figure 4. Schematic illustration of the nanowire-based device fabricated for FET and I-V photocurrent measurements (a) Optical microscopy image showing the $MAPbI_3$ nanowires crossing the Pt source-drain contacts deposited by e-beam evaporation (b). Dark and laser illuminated I-V curves under increasing laser power (c). Time-resolved photoresponse (d).

We measured the current density in the device as a function of the applied source-to-drain electric field in the dark and under illumination (red laser, $\lambda=633$ nm). The output characteristics follow a linear behavior, indicating that the contacts are ohmic (Fig 4 c). (The contacts show a slight asymmetric behavior probably due to fabrication asymmetries).

In the dark state, the device behaves like a good insulator with currents of the order of tens of pA and resistances in the GOhm range. Under the illumination of the laser, the absorption of the light generates electron-hole pairs that are extracted by the source-to-drain electric field and cause an increase in the conductance of the material up to a factor of 300. We probed the photoresponse of the device under different incident laser powers in the 70 nW to 7 µW range. The current increases parabolically with the incident power, however, under the applied experimental conditions the saturation of the photocurrent was not reached (inset to Fig 4 c).

The device configuration allows to test the effect of a gate electric field on the I-V characteristics. Despite the semiconducting nature of the material, no influence of gating was noticed (FigS12). The applicable electric field limit (break-down voltage) was determined to be ≈20kV/cm. Higher electric fields risk an irreversible rupture of the filiform crystallites (FigS13).

From the photocurrent one can estimate the responsivity of the device defined as $R = I_{ph}/P_{in}$, where I_{ph} is the photocurrent and P_{in} is the power of the incident light, respectively. For our device R was calculated to be 5 mA/W. Although this value is about 4 orders of magnitude smaller than the best-in-class photoelectric devices made out of graphene and monolayer

MoS_2[31,32,33,34], it is still comparable (10 times higher) to the value that has been achieved with the first prototypes of those 2D materials[35,36](Chart S1). Optimization of the device fabrication process and the engineering of its configuration might improve the performances of the photodetectors based on filiform perovskites.

The response time of our device (Fig 4d) showed that rise and decay times for the on-off current under illumination are less than 500µs, $\sim10^4$ faster than the state-of-the-art photodetectors made of monolayer MoS_2 [31,33] and graphene[32,34,37]. The stability of the device was also tested by performing ~100 consecutive cycles measured over 1 h (Fig S14). A slight increase of the photocurrent (~5 %) over time is presumably due to contact adjustments (a better interface is created with the metal trough some annealing mechanism, FigS14). In recent studies several groups[38-40] working on perovskite-based solar cells have reported a slight increase of Jsc (short-circuit current) after sequential measurements of light conversion efficiency or in the first hours of light instability tests. It has been suggested that the slight increase of the photocurrent could be the result of ionic charge transport, ion intercalation, or it might even be a ferroelectric effect. Deeper electrical and electro-optical characterization is needed to establish the exact mechanisms.

1
2
3
4
5
6
7
8
9
10
11
12
13
14
15
16
17
18
19
20
21
22
23
24
25
26
27
28
29
30
31
32
33
34
35
36
37
38
39
40
41
42
43
44
45
46
47
48
49
50
51
52
53
54
55
56
57
58
59
60

To compare the performance of the wire structure (Figure 5a, upper panel) with respect to the spin-coated film used today in solar cells, a photodetector with a film of $MAPbI_3$ nanoparticles was produced (Figure 5a, lower panel). Figure 5b gives the current density (calculated with the corresponding geometrical factors, details are in the Supplementary information) as a function of the source-drain voltage. The dark current measurements revealed that the flow of charge carriers is facilitated in the coating composed of $MAPbI_3$ nanoparticles slip-coated from GBL solution. The photocurrent-dark current ratio under a laser intensity of 2.5 Wcm^{-2} (λ=633nm) increases exponentially for the elongated perovskites, while the increase is almost linear for the nanoparticles (Fig 5c). The photocurrent-dark current ratio is one order of magnitude higher for filiform crystallites applying 1kV/cm electric field. The performance limitations in the nanoparticle based film (most probably due to the increased number of grain boundaries) are also observable from the external quantum efficiency (EQE) defined as Rhν/e (details are in Supplementary information). For low voltages (<0.5V) the EQE of the device made of fibrous perovskites is twice as high as the photodetector prepared from $MAPbI_3$ nanoparticles.
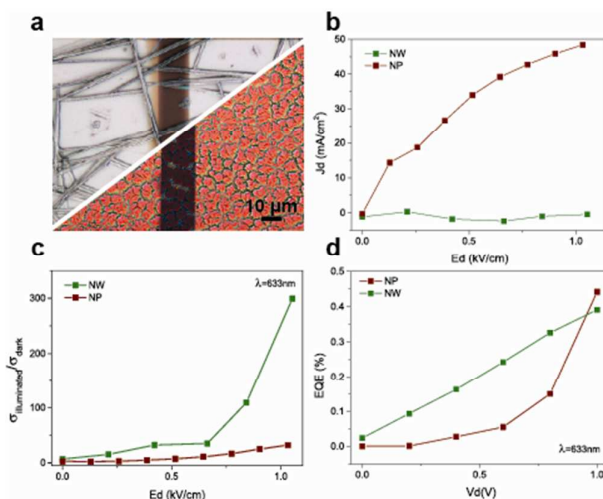
Figure 5. (a) Combined SEM-optical micrographs showing the surface of the thin film composed of nearly isotropic MAPbI$_3$ particles (bottom) and nanowires (top) with the Pt source-drain contacts deposited by e-beam evaporation (a). The grain boundaries in the nanoparticle-based film are clearly perceivable with a green-blue color (a, bottom). Note the absence of such a contrast in the case of filiform perovskites (a, top). Comparison of the dark current density of the nanoparticle and nanowire based devices (b). Comparison of the photocurrent-dark current ratio of the nanoparticle and nanowire based devices (c). Comparison of the external quantum efficiency of the nanoparticle and nanowire based devices (d).

These results demonstrate that the morphological properties, such as the crystallite size, form and its orientation could play an essential role in the photodetection and photoconductive response of the trihalide perovskite thin films.

Conclusion

Lead-methylamine iodide in a photovoltaic configuration with a very simple processing has already demonstrated 16% light conversion efficiency. One can hope We hypothesize that improving the materials properties could increase the upper limits of this conversion. Keeping in mind dye-sensitized solar cells with solid state electrolyte, where the replacement of TiO_2 nanoparticles with nanowires has considerably improved efficiency, we have developed the synthesis of $MAPbI_3$ nanowires. Their transport (photophysical) characteristics supersede those of isotropic nanocrystal-based thin films used in current devices. The relevant example, that recrystallization from solvents of different nature facilitates forming of elongated solvatomorphs of lead-methylamine iodide gives an opportunity to realize new solution-mediated strategies with the ultimate goal of exerting control over crystallite characteristics. The optically active elongated form of trihalide perovskites will make it

possible to explore exciting opportunities in the photonics industry such as solar energy conversion, photodetectors, light-emitting diodes and on-chip coherent light sources.

AUTHOR INFORMATION

Corresponding Author

Dr. Endre Horváth. Mail: endre.horvath@epfl.ch. Tel.: +41 21 69 34515. Fax: +41 21 693 4470.

References

1.   He, T.; Huang, Q.; Ramirez, A. P.; Wang, Y.; Regan, K. A.; Rogado, N.; Hayward, M. A.; Haas, M. K.; Slusky, J. S.; Inumara, K.; Zandbergen, H. W.; Ong, N. P.; Cava, R. J. *Nature* **2001,** 411, (6833), 54-56.

2.   Shimizu, Y.; Fukuyama, Y.; Arai, H.; Seiyama, T., Oxygen Sensor Using Perovskite-Type Oxides. In *Fundamentals and Applications of Chemical Sensors*, American Chemical Society: 1986; Vol. 309, pp 83-100.

3.   Boukamp, B. A. *Nat Mater* **2003,** 2, (5), 294-296.

4.   Pytte, E. *Phys Rev B* **1972,** 5, (9), 3758-&.

5.   Bocher, L.; Aguirre, M. H.; Logvinovich, D.; Shkabko, A.; Robert, R.; Trottmann, M.; Weidenkaff, A. *Inorg Chem* **2008,** 47, (18), 8077-8085.

6.   Zhang, A.; Cheng, J.; Kim, H.; Liu, Y. S.; Lo, Y. H. *Quantum Sensing and Nanophotonic Devices Vii* **2010,** 7608.

7.   Kojima, A.; Teshima, K.; Shirai, Y.; Miyasaka, T. *J Am Chem Soc* **2009,** 131, (17), 6050-6051.

8.   Liu, C.-H.; Chang, Y.-C.; Norris, T. B.; Zhong, Z. *Nat Nano* **2014,** advance online publication.

9.   Mosconi, E.; Amat, A.; Nazeeruddin, M. K.; Grätzel, M.; De Angelis, F. *The Journal of Physical Chemistry C* **2013,** 117, (27), 13902-13913.

10.   Kim, H.-S.; Lee, C.-R.; Im, J.-H.; Lee, K.-B.; Moehl, T.; Marchioro, A.; Moon, S.-J.; Humphry-Baker, R.; Yum, J.-H.; Moser, J. E.; Gratzel, M.; Park, N.-G. *Sci. Rep.* **2012,** 2.

11.   Docampo, P.; Ball, J. M.; Darwich, M.; Eperon, G. E.; Snaith, H. J. *Nat Commun* **2013,** 4.

12.   Xing, G.; Mathews, N.; Sun, S.; Lim, S. S.; Lam, Y. M.; Grätzel, M.; Mhaisalkar, S.; Sum, T. C. *Science* **2013,** 342, (6156), 344-347.

13.   Im, J.-H.; Lee, C.-R.; Lee, J.-W.; Park, S.-W.; Park, N.-G. *Nanoscale* **2011,** 3, (10), 4088-4093.

14.   Stranks, S. D.; Eperon, G. E.; Grancini, G.; Menelaou, C.; Alcocer, M. J. P.; Leijtens, T.; Herz, L. M.; Petrozza, A.; Snaith, H. J. *Science* **2013,** 342, (6156), 341-344.

15.   Colella, S.; Mosconi, E.; Fedeli, P.; Listorti, A.; Gazza, F.; Orlandi, F.; Ferro, P.; Besagni, T.; Rizzo, A.; Calestani, G.; Gigli, G.; De Angelis, F.; Mosca, R. *Chem Mater* **2013,** 25, (22), 4613-4618.

16.   Edri, E.; Kirmayer, S.; Henning, A.; Mukhopadhyay, S.; Gartsman, K.; Rosenwaks, Y.; Hodes, G.; Cahen, D. *Nano Lett* **2014,** 14, (2), 1000-1004.

17.   Pang, S.; Hu, H.; Zhang, J.; Lv, S.; Yu, Y.; Wei, F.; Qin, T.; Xu, H.; Liu, Z.; Cui, G. *Chem Mater* **2014,** 26, (3), 1485-1491.

18.   Noh, J. H.; Im, S. H.; Heo, J. H.; Mandal, T. N.; Seok, S. I. *Nano Lett* **2013,** 13, (4), 1764-1769.

19.   Kulkarni, S. A.; Baikie, T.; Boix, P. P.; Yantara, N.; Mathews, N.; Mhaisalkar, S. G. *J Mater Chem A* **2014**.

20.   Im, J.-H.; Chung, J.; Kim, S.-J.; Park, N.-G. *Nanoscale Res Lett* **2012,** 7, (1), 353.

21.   Ball, J. M.; Lee, M. M.; Hey, A.; Snaith, H. J. *Energy & Environmental Science* **2013,** 6, (6), 1739-1743.

22.   Burschka, J.; Pellet, N.; Moon, S.-J.; Humphry-Baker, R.; Gao, P.; Nazeeruddin, M. K.; Gratzel, M. *Nature* **2013,** 499, (7458), 316-319.

23.   Wojciechowski, K.; Saliba, M.; Leijtens, T.; Abate, A.; Snaith, H. J. *Energy & Environmental Science* **2014,** 7, (3), 1142-1147.

24.   Eperon, G. E.; Burlakov, V. M.; Docampo, P.; Goriely, A.; Snaith, H. J. *Adv Funct Mater* **2014,** 24, (1), 151-157.

25.   Liu, M.; Johnston, M. B.; Snaith, H. J. *Nature* **2013,** 501, (7467), 395-398.

26.   Qin, P.; Domanski, A. L.; Chandiran, A. K.; Berger, R.; Butt, H.-J.; Dar, M. I.; Moehl, T.; Tetreault, N.; Gao, P.; Ahmad, S.; Nazeeruddin, M. K.; Gratzel, M. *Nanoscale* **2014,** 6, (3), 1508-1514.

27.   Baikie, T.; Fang, Y.; Kadro, J. M.; Schreyer, M.; Wei, F.; Mhaisalkar, S. G.; Graetzel, M.; White, T. J. *J Mater Chem A* **2013,** 1, (18), 5628-5641.

28.   Quarti, C.; Grancini, G.; Mosconi, E.; Bruno, P.; Ball, J. M.; Lee, M. M.; Snaith, H. J.; Petrozza, A.; Angelis, F. D. *The Journal of Physical Chemistry Letters* **2013,** 5, (2), 279-284.

29.   Lee, M. M.; Teuscher, J.; Miyasaka, T.; Murakami, T. N.; Snaith, H. J. *Science* **2012,** 338, (6107), 643-647.

30.   Xing, G.; Mathews, N.; Lim, S. S.; Yantara, N.; Liu, X.; Sabba, D.; Grätzel, M.; Mhaisalkar, S.; Sum, T. C. *Nat Mater* **2014,** advance online publication.

31.   Zhang, W. J.; Chuu, C. P.; Huang, J. K.; Chen, C. H.; Tsai, M. L.; Chang, Y. H.; Liang, C. T.; Chen, Y. Z.; Chueh, Y. L.; He, J. H.; Chou, M. Y.; Li, L. J. *Sci Rep-Uk* **2014,** 4.

32.   Jin, W.; Gao, Z.; Zhou, Y.; Yu, B.; Zhang, H.; Peng, H.; Liu, Z.; Dai, L. *Journal of Materials Chemistry C* **2014,** 2, (9), 1592-1596.

33.   Lopez-Sanchez, O.; Lembke, D.; Kayci, M.; Radenovic, A.; Kis, A. *Nat Nano* **2013,** 8, (7), 497-501.

34. Konstantatos, G.; Badioli, M.; Gaudreau, L.; Osmond, J.; Bernechea, M.; de Arquer, F. P. G.; Gatti, F.; Koppens, F. H. L. *Nat Nano* **2012,** 7, (6), 363-368.
35. Xia, F. N.; Mueller, T.; Lin, Y. M.; Valdes-Garcia, A.; Avouris, P. *Nat Nanotechnol* **2009,** 4, (12), 839-843.
36. Yin, Z. Y.; Li, H.; Li, H.; Jiang, L.; Shi, Y. M.; Sun, Y. H.; Lu, G.; Zhang, Q.; Chen, X. D.; Zhang, H. *Acs Nano* **2012,** 6, (1), 74-80.
37. Zhang, Y. Z.; Liu, T.; Meng, B.; Li, X. H.; Liang, G. Z.; Hu, X. N.; Wang, Q. J. *Nature Communications* **2013,** 4.
38. Dualeh, A.; Moehl, T.; Tétreault, N.; Teuscher, J.; Gao, P.; Nazeeruddin, M. K.; Grätzel, M. *Acs Nano* **2013,** 8, (1), 362-373.
39. Sanchez, R. S.; Gonzalez-Pedro, V.; Lee, J.-W.; Park, N.-G.; Kang, Y. S.; Mora-Sero, I.; Bisquert, J. *The Journal of Physical Chemistry Letters* **2014,** 5, (13), 2357-2363.
40. Leijtens, T.; Eperon, G. E.; Pathak, S.; Abate, A.; Lee, M. M.; Snaith, H. J. *Nat Commun* **2013,** 4.